

Advancing automated pupillometry: a practical deep learning model utilizing infrared pupil images

Dai Guangzheng^{1,3}, Yu Sile¹, Liu Ziming^{2,4}, Yan Hairu², He Xingru¹

引用:代光政,余斯乐,刘子铭,等. 创新自动瞳孔测量技术:基于红外瞳孔图像的深度学习模型.国际眼科杂志, 2024,24(10): 1522-1528.

Foundation item: The General Program of Educational Department of Liaoning Province (No.LJKZ1387)

¹School of Public Health, He University, Shenyang 110000, Liaoning Province, China; ²School of Artificial Intelligence and Big Data, He University, Shenyang 110000, Liaoning Province, China; ³Clinical Research Center, He Eye Specialist Hospital, Shenyang 110000, Liaoning Province, China; ⁴The Graduate School, Liaoning University of Traditional Chinese Medicine, Shenyang 110000, Liaoning Province, China

Correspondence to: He Xingru. School of Public Health, He University, Shenyang 110000, Liaoning Province, China. hexingru@huh.edu.cn

Received: 2023-04-04 Accepted: 2024-05-29

创新自动瞳孔测量技术:基于红外瞳孔图像的深度学习模型

代光政^{1,3},余斯乐¹,刘子铭^{2,4},闫海茹²,何星儒¹

基金项目:辽宁省教育厅面上项目(No.LJKZ1387)

作者单位:¹(110000)中国辽宁省沈阳市,辽宁何氏医学院公共卫生学院;²(110000)中国辽宁省沈阳市,辽宁何氏医学院人工智能与大数据学院;³(110000)中国辽宁省沈阳市,沈阳何氏眼科医院有限公司临床研究部;⁴(110000)中国辽宁省沈阳市,辽宁中医药大学研究生院

作者简介:代光政,毕业于大连医科大学,博士研究生,副主任医师,研究方向:医学人工智能。

通讯作者:何星儒,毕业于约翰霍普金斯大学,博士研究生,副教授,研究方向:卫生经济评估.hexingru@huh.edu.cn

摘要

目的:建立基于红外图像的瞳孔直径测量算法,以便在实际临床环境中使用。

方法:纳入 2022-09/12 于沈阳何氏眼科医院门诊患者 188 例,共收集红外瞳孔图像 13 470 张。所有用于瞳孔分割的红外图像均使用 Labelme 软件进行标注。瞳孔直径的计算分为四个步骤:图像预处理、瞳孔识别与定位、瞳孔分割及直径计算。计算过程中使用修改后的 YoloV3 模型和 DeeplabV3+模型,这两个模型需要事先训练。

结果:测试数据集共 1 348 张红外瞳孔图像,修改后的 YoloV3 模型的检测率为 99.98%,瞳孔的平均精确度(AP)

为 0.80。DeeplabV3+模型达到了 99.23%的背景交并比(IOU),93.81%的瞳孔 IOU 和平均 96.52%的 IOU。测试数据集中瞳孔直径范围为 20 至 56 像素,平均为 36.06±6.85 像素。预测和实际值之间瞳孔直径的绝对误差范围为 0 至 7 像素,平均绝对误差(MAE)为 1.06±0.96 像素。

结论:本研究成功展示了一种基于红外图像的稳健瞳孔直径测量算法,证明该算法具有高度准确性和可靠性,适用于临床应用。

关键词:瞳孔;红外图像;算法;深度学习模型

Abstract

• **AIM:** To establish pupil diameter measurement algorithms based on infrared images that can be used in real-world clinical settings.

• **METHODS:** A total of 188 patients from outpatient clinic at He Eye Specialist Shenyang Hospital from Spetember to December 2022 were included, and 13 470 infrared pupil images were collected for the study. All infrared images for pupil segmentation were labeled using the Labelme software. The computation of pupil diameter is divided into four steps: image pre-processing, pupil identification and localization, pupil segmentation, and diameter calculation. Two major models are used in the computation process: the modified YoloV3 and Deeplabv 3+ models, which must be trained beforehand.

• **RESULTS:** The test dataset included 1 348 infrared pupil images. On the test dataset, the modified YoloV3 model had a detection rate of 99.98% and an average precision (AP) of 0.80 for pupils. The DeeplabV3+ model achieved a background intersection over union (IOU) of 99.23%, a pupil IOU of 93.81%, and a mean IOU of 96.52%. The pupil diameters in the test dataset ranged from 20 to 56 pixels, with a mean of 36.06±6.85 pixels. The absolute error in pupil diameters between predicted and actual values ranged from 0 to 7 pixels, with a mean absolute error (MAE) of 1.06±0.96 pixels.

• **CONCLUSION:** This study successfully demonstrates a robust infrared image-based pupil diameter measurement algorithm, proven to be highly accurate and reliable for clinical application.

• **KEYWORDS:** pupil; infrared image; algorithm; deep learning model

DOI:10.3980/j.issn.1672-5123.2024.10.02

Citation: Dai GZ, Yu SL, Liu ZM, et al. Advancing automated pupillometry: a practical deep learning model utilizing infrared pupil images. Guoji Yanke Zazhi (Int Eye Sci), 2024, 24(10): 1522-1528.

INTRODUCTION

The pupil, situated at the core of the iris, is crucial for regulating light entry into the eye. Its dynamic adjustment of diameter^[1], vital for visual function, is controlled by the coordinated actions of the pupillary sphincter and dilator muscles in response to light and other stimuli^[2-3]. Consequently, abnormalities in pupillary responses can reveal important information about diverse medical conditions, rendering precise pupil size measurement a vital diagnostic instrument^[4-5].

Accurately delineating the dynamic fluctuations in pupil size necessitates both precision and real-time tracking. The pupil gauge remains the favored tool in clinical settings due to its straightforward application. Yet, it falls short for continuous and precise dynamic assessments, as it fails to visually quantify the rates of pupil constriction or expansion^[6]. Alternative instruments, not originally designed for pupillometry – such as wavefront aberrometers and corneal topographers – can furnish more accurate measures. Wavefront aberrometry provides static insights but lacks the capability for ongoing monitoring of the light – adaptive pupil^[7-8]. In contrast, corneal topography boasts high computational accuracy and consistency, enabling the observation of pupil dynamics in response to illumination^[9-10]. Nevertheless, this method is contingent on a controlled lighting backdrop and is ineffective for capturing pupillary responses in darkened conditions.

Infrared imaging technology facilitates the generation of high-quality images of the pupil^[11]. The predominant algorithms for determining pupil diameter from such images typically leverage traditional image processing techniques, lauded for their speed, interpretability, and low computational demands. Yet, their major drawback lies in the inadequate accuracy when measuring pupils with non – standard geometries. Clinically, such irregular shapes are not uncommon and include semi – circular pupils from eyelid droop (ptosis), pinpoint pupils due to organophosphorus poisoning, and distortions following iris surgery, among others. The advent and evolution of artificial intelligence in recent years have broadened its application in the field of ophthalmology, yielding a host of significant advancements^[12-14]. This study harnesses infrared imaging to obtain pupil visuals alongside deep learning algorithms to determine pupil diameter, ensuring precision and adherence to the real-time constraints of clinical pupil assessments.

SUBJECTS AND METHODS

Ethical Approval This study adhered to the tenets of the Declaration of Helsinki and received He University's Institutional Review Board approval (IRB (2022) K001.01). All participants furnished written informed consent prior to inclusion.

Data Collection Figure 1 illustrates the setup for capturing infrared pupil images in this study, utilizing the Eyerobo VS

(eyeROBO Co., Ltd.). This device features an external tube, one meter in length, to ensure a constant shooting distance and to create an adequately dark environment for capturing images. The core components of the infrared camera system are an infrared light source and a digital camera, as demonstrated in Figure 2. The imaging principle involves infrared light reflecting off the retina, creating a distinct luminous region within the pupil. The digital camera boasts a 0.3-megapixel resolution and is equipped with a 64 MB cache to enhance the speed and reliability of data transfer.

Participants were enrolled from the outpatient clinic at He Eye Specialist Shenyang Hospital during the period from September to December 2022. The collection of infrared pupil images was carried out by two expertly trained technicians. During the imaging process, patients maintained proximity to the device's eyecup, fixating on a visual target with eyes widely opened, avoiding blinking, eye movements, or head adjustments. The selection criteria for the images specified that each must capture more than one half of the pupil and that the grayscale intensity of the pupil must surpass that of the iris; images failing to meet these standards were discarded. The final cohort consisted of 188 individuals, yielding a total of 13 470 infrared pupil images, documenting diverse ocular conditions, which included healthy eyes as well as those with cataracts, glaucoma, artificial intraocular lenses, aphakia, refractive errors, vitreous hemorrhage, diabetic retinopathy, entropion, among others, and even cases with indeterminate diagnoses. Illustrated in Figure 3A, each image included both eyes, had

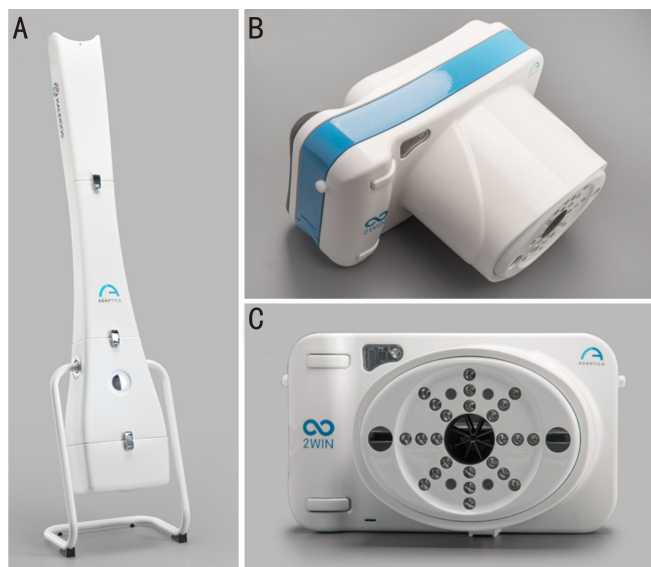


Figure 1 Infrared image acquisition apparatus for pupils. A: External tube; B and C: Internal infrared camera.

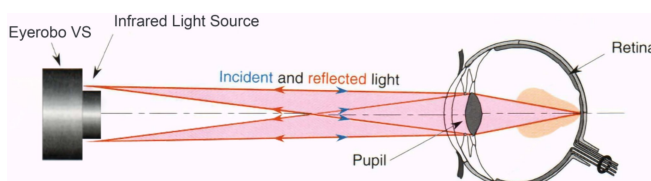


Figure 2 The principle of imaging the pupillary area.

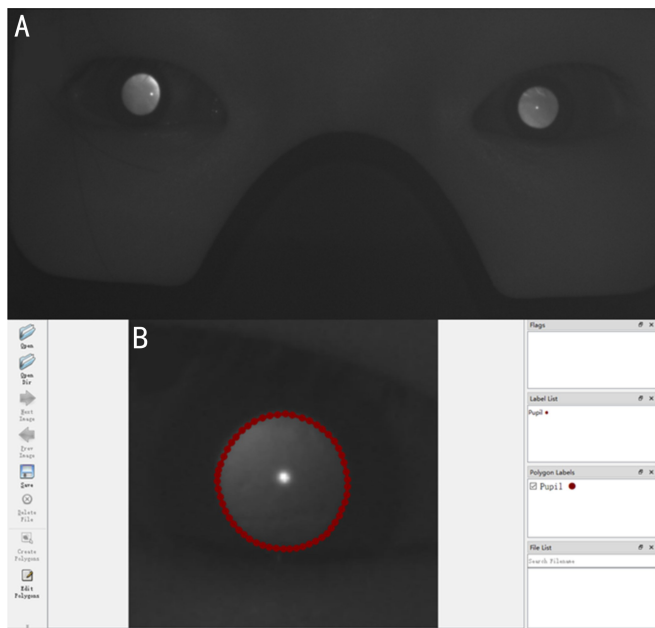


Figure 3 Infrared image of the pupil. A: Original image; B: Labeled image.

dimensions of 752 by 360 pixels, and featured a resolution of 96 dpi. This extensive image collection was then systematically segregated into three subsets for model training (8 484 images), validation (3 638 images), and final testing (1 348 images).

Data Annotation LabelMe software facilitated the annotation of all infrared pupil images, as illustrated in Figure 3B. Effective pupil labeling adheres to the following criteria: the labeling points must be smooth, dense, and continuous; furthermore, they must align precisely with the pupil's periphery. The annotation process unfolds in 3 distinct steps: initially, an algorithm engineer designs the labeling protocol and produces a tutorial video. This video is then disseminated to the annotators, encompassing clinical medical interns, vision function specialists, and ophthalmologists, who upon review, are primed to discuss any concerns with the creators. Subsequently, a trio of ophthalmologists rigorously examines the labeled data, returning any inadequate examples for refinement. These meticulously annotated images are instrumental in determining the pupil diameter, which is quantified by the widest pupil horizontal span and acts as the standard for evaluating the algorithm posited in this research. Table 1 outlines the distribution properties of the pupil diameters across the 13 470 infrared pupil images.

Algorithm Development Figure 4 illustrates the methodology for calculating pupil diameter, comprising 4 key steps: image pre-processing, locating and identifying the pupil, segmenting the pupil, and computing the diameter. To individually process the images of the left and right pupils, the photograph is divided vertically down the center to create 2 equal halves, each trimmed to dimensions of 360 by 360 pixels. The bounding box deemed most reliable encapsulates the region harboring the pupil, from which the precise center

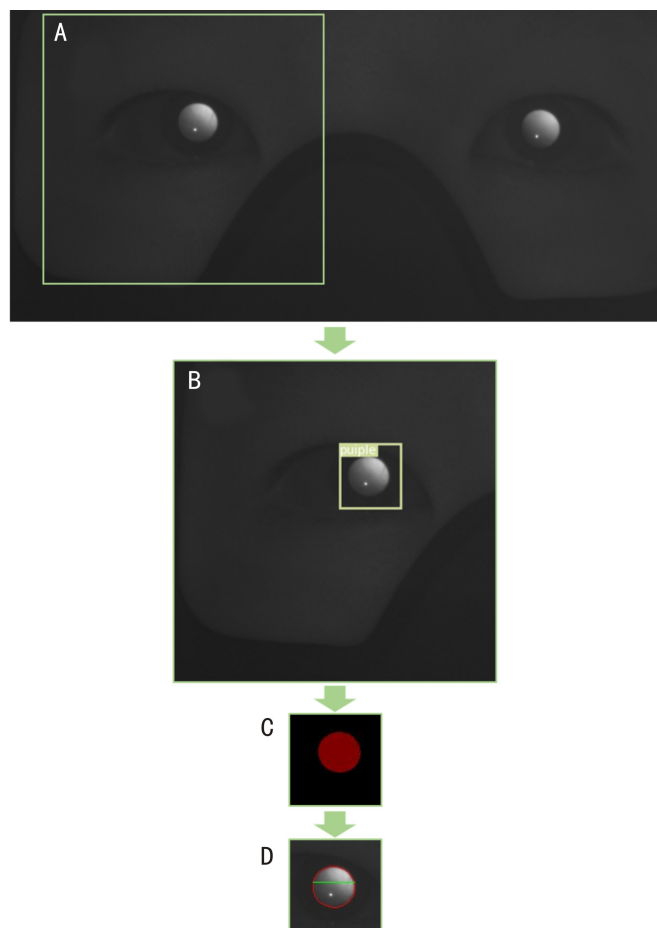


Figure 4 Procedures for calculating pupil diameter. A: Original image; B: Pupil localization; C: Pupil segmentation; D: Pupil diameter calculation.

is determined. Centered on this specific coordinate, a 100 by 100 - pixel area representing the pupil is extracted. This isolated segment of the pupil image is then used to ascertain the pupil's maximum horizontal extent, defining its diameter. The computational procedure requires the preliminary training of two crucial models. An adapted YoloV3^[15] is employed for pupil detection and positioning, trained on 360×360 pixel images. YoloV3-You Only Look Once, version 3-is a state-of-the-art, real-time object detection framework that simultaneously identifies and categorizes objects within a single network pass. It employs Darknet-53, a 53-layer deep convolutional neural network architecture pre-trained on the ImageNet dataset, enabling it to discern a broad spectrum of features. Model modifications include the adoption of a single output header due to the uniform pupil size, utilization of the K-MEANS^[16] clustering algorithm to determine anchor boxes measuring 38×38, 35×27, and 45×46 pixels tailored to the dataset's pupil size distribution, and the retention of only the most confident detection box per image with a single pupil. YoloV3's integration into our algorithm facilitates the rapid and accurate localization of the pupil in images, a critical feature for time-sensitive clinical applications. The Deeplabv3+^[17] model, integrating the MobileNetV2^[18] architecture, was utilized for pupil segmentation, trained on

Table 1 Characteristics of the pupil diameter data (n = 13 470)

Conditions	Number (%)	Mean diameter ($\bar{x} \pm s$, px)	Minimum diameter (px)	Maximum diameter (px)
Normal	2 998 (22.26%)	45.10±4.56 ^a	29	56
Cataract	4 579 (33.99%)	32.77±4.22 ^b	19	47
Glaucoma	181 (1.34%)	27.12±4.86 ^b	16	33
Intraocular lens	531 (3.94%)	35.17±4.22 ^b	7	42
Aphakic eye	48 (0.36%)	30.31±1.62 ^b	25	33
Refractive error	399 (2.96%)	34.71±4.10 ^b	26	42
Vitreous hemorrhage	23 (0.17%)	24.86±1.36 ^b	22	27
Diabetic retinopathy	92 (0.68%)	32.40±1.39 ^b	29	35
Entropion	78 (0.58%)	36.65±1.89 ^b	33	41
Unknown	4 541 (33.71%)	33.43±5.25 ^b	19	57

Normal; Without ocular disease; Unknown; With untraceable ocular diagnoses; ^a Reference group; ^b Using the normal group as a reference, there was a statistical difference after Bonferroni correction ($P < 0.01$).

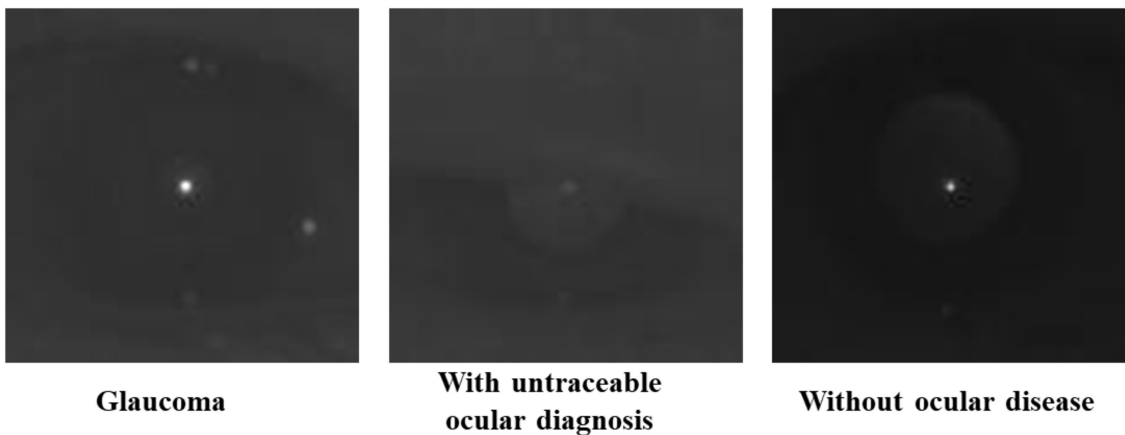


Figure 5 Three infrared images where the pupil was not detected.

100x100 pixel images. As an advancement in the Deeplab series, Deeplabv3 + specializes in semantic image segmentation, which involves dividing an image into meaningful portions and categorizing each into predefined classes. It features an encoder–decoder framework with atrous convolutions, optimizing the feature response resolution in Deep Convolutional Neural Networks. Furthermore, Deeplabv3+ incorporates an atrous spatial pyramid pooling (ASPP) module for effectively segmenting objects on various scales and assimilating extensive contextual data. Within our algorithm, Deeplabv3 + is employed to define the pupil’s contours precisely, an essential step for the accurate measurement of pupil diameter, particularly in the infrared image domain where challenging conditions are prevalent.

To appraise conventional pupil measurement techniques, this investigation harnessed the HoughCircle transform^[19–20] alongside the Watershed algorithm^[21] to gauge pupil dimensions. The Watershed and HoughCircles utilities from OpenCV were instrumental in this analysis. In particular, for the HoughCircles function, vital parameters were meticulously chosen to optimize the rate and precision of pupil identification, namely: method = cv2.HOUGH_GRADIENT_ALT, minDist = 40, param1 = 38, param2 = 0.7, minRadius = 7, and maxRadius = 31. These parameters have been

established based on a statistical analysis of annotated pupil imagery. The study truncated infrared pupil photographs to dimensions of 100 by 100 pixels for the empirical comparison of three distinct methods; Deeplabv3+, HoughCircles, and Watershed.

The development of the algorithms was carried out using Python 3.6, complemented by libraries including OpenCV 4.5 and PyTorch 1.12.

Algorithm Evaluation To assess the efficacy of pupil detection, localization, and segmentation, this study utilized metrics such as the detection rate, average precision (AP), and intersection over union (IOU). AP, denoting the area beneath the precision–recall curve, is a robust indicator of detection accuracy; values nearing unity suggest superior detection precision and recall. The IOU metric, defined as the ratio of the overlap between the predicted result and the ground truth to their combined area, reveals the extent of agreement with values approaching unity signifying greater alignment. Additionally, the study employed mean absolute error (MAE) to measure the discrepancy in pupil diameters; a minimized MAE corresponds to more accurate diameter estimations.

RESULTS

The test set, comprising 1 348 pupil images, was processed in

39 seconds, yielding a computation speed of 34.6 images per second. The refined YoloV3 model excelled, identifying 1 345 pupils accurately, with a detection rate of 99.98% and an AP of 0.80. Figure 5 illustrates three infrared images—one each from cases without ocular disease, with glaucoma, and with an indeterminate ocular diagnosis—showcasing instances where pupil detection failed due to grey values in the pupil area approximating those of the surrounding iris. In terms of segmentation performance, the DeeplabV3+ model attained a background IOU of 99.23%, a pupil IOU of 93.81%, and an average IOU of 96.52%. Pupil diameters in the test set varied from 20 to 56 pixels, averaging 36.06 ± 6.85 pixels. The range of absolute errors in estimated pupil diameters compared to actual measurements spanned from 0 to 7 pixels, with a MAE of 1.06 ± 0.96 pixels.

Measurement errors in the diameter of infrared pupil images were stratified by disease type, with findings detailed in Table 2. Notably, the glaucoma group demonstrated a higher MAE relative to the cataract, artificial intraocular lens, refractive error groups, and those without definitive ocular diagnoses, with these variances being statistically significant. Pupil measurements were conducted on 1 348 infrared images, each sized at 100 by 100 pixels, utilizing three distinct techniques: Hough Circle Transform, Watershed algorithm, and DeeplabV3+, with the respective outcome data presented in Table 3. Among these methods, DeeplabV3+ had the superior performance, whereas the Watershed algorithm yielded the least favorable results.

DISCUSSION

The Eyerobo VS was selected as the imaging apparatus for its uniquely designed external tube, which standardizes the

capture of infrared pupil images. This tube assures a uniform dark setting, a key requirement given the pivotal influence of ambient light on pupil size, and establishes a definitive detection range by maintaining a fixed one-meter distance between the subject's eye and the infrared camera. Consequently, this uniformity allows for reproducible measurements across different subjects or sequential evaluations for the same individual. By capitalizing on the collective strengths of various algorithms and synthesizing them, our approach augments the accuracy and detection efficacy of pupil diameter assessments in practical medical settings.

The process for computing the pupil diameter entails a structured algorithmic approach. As a first step, images lacking a discernible pupil are excluded, considering the myriad clinical conditions that may impede proper capture: obstructive eyelids, patient movement, misalignment of the subject's eyes, or inopportune eye motion during the procedure. Following the exclusion, the remaining images undergo target recognition for initial pupil localization, after which the pertinent region is resized to 100×100 pixels to facilitate precise delineation in later stages. Subsequently, segmentation isolates the pupil from its background, leading to the final measurement of the broadest pupil horizontal span. This study's foremost benefit lies in its ability to precisely measure an extensive array of pupils with atypical shapes, as depicted in Figure 6. Variations include diminutive pupils, those partially obscured by one or both eyelids, those presenting irregular contours, and those not fully captured. Two factors primarily contribute to this capability: first, the data originate from genuine clinical environments, embracing

Table 2 Comparison of pupil measurement errors by disease type

(n = 1 345)

Conditions	Number (%)	MAE ($\bar{x} \pm s$, px)	Minimum (px)	Maximum (px)
Normal	318 (23.64%)	1.17±1.04	0	7
Cataract	456 (33.90%)	1.00±0.89 ^b	0	4
Glaucoma	20 (1.49%)	1.80±1.43 ^a	0	5
Intraocular lens	55 (4.09%)	0.90±1.00 ^b	0	6
Aphakic eye	6 (0.45%)	2.00±1.26 ^c	1	4
Refractive error	51 (3.79%)	0.82±0.71 ^b	0	3
Vitreous hemorrhage	1 (0.07%)	1.00±0.00 ^c	1	1
Diabetic retinopathy	7 (0.52%)	1.71±1.38 ^c	0	3
Trichiasis	6 (0.45%)	2.00±1.26 ^c	1	4
Unknown	425 (31.60%)	0.99±0.89 ^b	0	5

Normal: Without ocular disease; Unknown: With untraceable ocular diagnosis; MAE: Mean absolute error; ^a Reference group; ^b Using the glaucoma group as a reference, there was a statistical difference after Bonferroni correction ($P < 0.01$); ^c Because these groups had smaller samples, they were excluded from the statistical analysis.

Table 3 A comparative analysis of the performance of three algorithms

(n = 1 348)

Algorithms	Proportion (%)	Pupil IOU (%)	Background IOU (%)	Mean IOU (%)	MAE ($\bar{x} \pm s$, px)
Deeplabv3+	100.00	93.41	99.21	96.31	0.97±0.95
HoughCircle	92.67	79.26	97.30	88.28	2.37±2.41
Watershed	86.79	36.60	79.50	58.05	27.63±25.38

Proportion: The proportion of successfully calculated pupil diameter; IOU: Intersection over union; MAE: Mean absolute error.

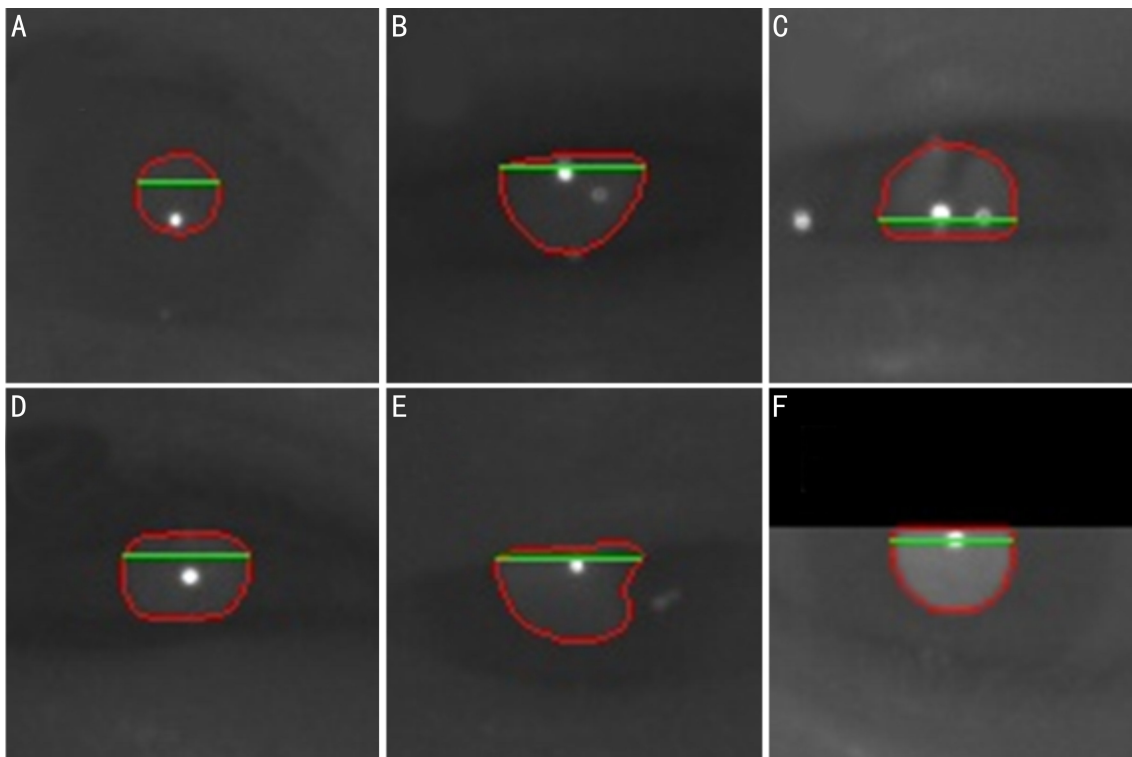


Figure 6 Infrared images of pupils with abnormal pupil shape. A: Pupil that are smaller than typical; B: Pupil obscured by the upper eyelid; C: Pupil obscured by the upper eyelid; D: Pupils with irregular shapes; E: Pupil obscured by the upper eyelid; F: Pupil that were not photographed intact.

a spectrum of eye diseases, which furnishes a collection of pupils with heterogeneous forms. Second, the employment of deep learning surpasses traditional image processing in analyzing diverse pupil figures with improved accuracy.

The algorithm developed in this investigation surpasses traditional pupil measurement techniques, including the Watershed and HoughCircle detection methods, across all evaluated metrics. Conventionally, image processing algorithms depend on handcrafted feature extractors tailored for specific applications, demanding expert knowledge and intricate adjustments, yet often lacking in adaptability and durability^[22]. Practical imaging conditions introduce variability in aspects such as lighting, image quality, and pupil shape, prompting frequent failures in legacy algorithms under certain circumstances. Contrarily, deep learning obviates the need for manual feature crafting by concurrently assimilating all characteristics, thereby markedly streamlining the analytical workflow and favoring an efficient end-to-end model over convoluted traditional approaches^[23]. Within the scope of this research, the YoloV3 and Deeplabv3+ models – established and prevalent in engineering applications – were selected for their proven utility. Despite the availability of advanced instance segmentation and object recognition models like InternImage-H^[24], ViT-Adapter^[25], Mask2Former^[26], Co-DETR^[27], MoCaE^[28], DyHead^[29], these were not employed in the current study. The exclusion was based on 2 primary reasons: first, the algorithms assessed herein adequately meet the clinical requirements for measuring pupil size; second, the implementation framework for the selected

models exhibits greater maturity.

Despite its strengths, this study acknowledges several limitations. Within a test set of 1 348 images, pupils in 3 cases went undetected, corresponding to subjects from the glaucoma group, the control group, and a group without a confirmed diagnosis. Figure 2 illustrates that these instances feature indistinguishable grayscale values between the pupil and adjacent iris, potentially causing the model's detection challenges. Moreover, measurements of glaucoma patients' pupil diameters exhibited higher error margins across the dataset. This may be attributed to two primary factors: the reduced pupil diameter in glaucoma patients^[30], which impacts measurement precision, and the underrepresentation of glaucoma images in the dataset, yielding inadequate training volumes for the model.

This study demonstrates the effectiveness of an automated pupil diameter measurement algorithm using infrared imaging. It has been validated for high accuracy, reliability, and real-time applicability in clinical environments. Notably, the algorithm's robustness is proven against diverse aberrant pupil morphologies frequently observed in clinical practice.

REFERENCES

- [1] Kahneman D, Beatty J. Pupil diameter and load on memory. *Science*, 1966, 154(3756):1583–1585.
- [2] Wilhelm H. Disorders of the pupil. *Handb Clin Neurol*, 2011, 102: 427–466.
- [3] Kardon R. Pupillary light reflex. *Curr Opin Ophthalmol*, 1995, 6(6):20–26.
- [4] Pinheiro HM, da Costa RM. Pupillary light reflex as a diagnostic aid

from computational viewpoint: a systematic literature review. *J Biomed Inform*, 2021,117:103757.

[5] Joshi S, Gold JI. Pupil size as a window on neural substrates of cognition. *Trends Cogn Sci*, 2020,24(6):466-480.

[6] Schmitz S, Krummenauer F, Henn S, et al. Comparison of three different technologies for pupil diameter measurement. *Graefes Arch Clin Exp Ophthalmol*, 2003,241(6):472-477.

[7] Bardak H, Gunay M, Bardak Y, et al. Evaluation of the acute changes in objective accommodation, pupil size and ocular wavefront aberrations after cigarette smoking. *Cutan Ocul Toxicol*, 2017,36(1):25-28.

[8] Wickremasinghe SS, Smith GT, Stevens JD. Comparison of dynamic digital pupillometry and static measurements of pupil size in determining scotopic pupil size before refractive surgery. *J Cataract Refract Surg*, 2005,31(6):1171-1176.

[9] Piñero DP. Technologies for anatomical and geometric characterization of the corneal structure and anterior segment: a review. *Semin Ophthalmol*, 2015,30(3):161-170.

[10] Periman LM, Ambrosio R Jr, Harrison DA, et al. Correlation of pupil sizes measured with a mesopic infrared pupillometer and a photopic topographer. *J Refract Surg*, 2003,19(5):555-559.

[11] Larson MD, Behrends M. Portable infrared pupillometry: a review. *Anesth Analg*, 2015,120(6):1242-1253.

[12] Betzler BK, Rim TH, Sabanayagam C, et al. Artificial intelligence in predicting systemic parameters and diseases from ophthalmic imaging. *Front Digit Health*, 2022,4:889445.

[13] Li JO, Liu HR, Ting DSJ, et al. Digital technology, tele-medicine and artificial intelligence in ophthalmology: a global perspective. *Prog Retin Eye Res*, 2021,82:100900.

[14] Wang JP, Yu MT, Xu BL, et al. Analysis of retinal arteriolar and venular parameters in primary open angle glaucoma. *Int J Ophthalmol*, 2023,16(5):671-679.

[15] Redmon J, Farhadi A. YOLOv3: an incremental improvement. 2018:1804.02767. <https://arxiv.org/abs/1804.02767v1>

[16] MacQueen J. Some methods for classification and analysis of multivariate observations. *Proc. Symp. Math. Statist. and Probability*, 5th, 1967.

[17] Yurtkulu SC, Şahin YH, Unal G. Semantic segmentation with extended DeepLabv3 architecture. 2019 27th Signal Processing and Communications Applications Conference (SIU), 2019:1-4.

[18] Sandler M, Howard A, Zhu ML, et al. MobileNetV2: inverted residuals and linear bottlenecks. 2018 IEEE/CVF Conference on Computer Vision and Pattern Recognition, 2018:4510-4520.

[19] Duda RO, Hart PE. Use of the Hough transformation to detect lines and curves in pictures. *Commun ACM*, 1972,15(1):11-15.

[20] M S, G N. Realization of human eye pupil detection system using canny edge detector and circular Hough transform technique. 2023 2nd International Conference on Applied Artificial Intelligence and Computing (ICAAIC), 2023:861-865.

[21] Vincent L, Soille P. Watersheds in digital spaces: an efficient algorithm based on immersion simulations. *IEEE Trans Pattern Anal Mach Intell*, 1991,13(6):583-598.

[22] O'Mahony N, Campbell S, Carvalho A, et al. Deep learning vs. traditional computer vision. *Advances in Intelligent Systems and Computing*. Cham; Springer International Publishing, 2019:128-144.

[23] Fan JQ, Ma C, Zhong YQ. A selective overview of deep learning. *Stat Sci*, 2021,36(2):264-290.

[24] Wang WH, Dai JF, Chen Z, et al. InternImage: exploring large-scale vision foundation models with deformable convolutions. 2023 IEEE/CVF Conference on Computer Vision and Pattern Recognition (CVPR), 2023:14408-14419.

[25] Chen Z, Duan YC, Wang WH, et al. Vision transformer adapter for dense predictions. 2022: 2205. 08534. <https://arxiv.org/abs/2205.08534v4>

[26] Cheng BW, Misra I, Schwing AG, et al. Masked-attention mask transformer for universal image segmentation. 2022 IEEE/CVF Conference on Computer Vision and Pattern Recognition (CVPR), 2022:1280-1289.

[27] Zong ZF, Song GL, Liu Y. DETRs with collaborative hybrid assignments training. 2023 IEEE/CVF International Conference on Computer Vision (ICCV), 2023:6725-6735.

[28] Oksuz K, Kuzucu S, Joy T, et al. MoCaE: mixture of calibrated experts significantly improves object detection. *ArXiv, abs/2309.14976*, 2023.

[29] Dai XY, Chen YP, Xiao B, et al. Dynamic head: unifying object detection heads with attentions. 2021 IEEE/CVF Conference on Computer Vision and Pattern Recognition (CVPR). June 20-25, 2021, Nashville, TN, USA. IEEE, 2021:7369-7378.

[30] Hahnenberger R. Anisocoria in untreated unilateral open-angle glaucoma. *Acta Ophthalmol*, 1984,62(1):135-141.